Giant, Anomalous Piezoimpedance in Silicon-on-insulator

H. Li, C.T.K. Lew, B.C. Johnson, J.C. Mccallum, S. Arscott, A.C.H. Rowe

Giant, Anomalous Piezoimpedance in Silicon-on-insulator

H. Li,[1] C.T.K. Lew,[2] B.C. Johnson,[2] J.C. McCallum,[3] S. Arscott,[4] and A.C.H. Rowe[1,*]

[1] *Physique de la Matière Condensée, École Polytechnique, CNRS, Université Paris-Saclay, 91128 Palaiseau, France*

[2] *Centre for Quantum Computation & Communication Technology, School of Physics,University of Melbourne, Melbourne, Victoria 3010, Australia*

[3] *School of Physics, University of Melbourne, Melbourne, Victoria 3010, Australia*

[4] *Institut d'Electronique, de Microélectronique et de Nanotechnologie, Université de Lille, CNRS, Avenue Poincaré, Cité Scientifique, 59652 Villeneuve d'Ascq, France*

(Received 17 October 2018; revised manuscript received 28 January 2019; published 3 April 2019)

A giant, anomalous piezoresponse of fully depleted silicon-on-insulator devices under mechanical stress is demonstrated by impedance spectroscopy. This piezoresponse strongly depends on the measurement frequency, ω, and consists of both a piezoresistance (PZR) and a piezocapacitance, whose maximum values are -1100×10^{-11} and -900×10^{-11} Pa^{-1}, respectively. These values should be compared with the usual bulk PZR in p-type silicon, 70×10^{-11} Pa^{-1}. The observations are well described by models of space-charge-limited hole currents in the presence of fast electronic traps having stress-dependent capture rates (ω_c) and emission rates. Under steady-state conditions (i.e., when $\omega \ll \omega_c$), where the impedance-spectroscopy measurements yield results that are directly comparable with those of previously published reports of PZR in depleted, silicon nano-objects, the overall piezoresponse is just the usual, bulk silicon PZR. Anomalous PZR is observed only under non-steady-state conditions when $\omega \approx \omega_c$, with a symmetry suggesting that the electromechanically active fast traps are native Pb_0 interface defects. The observations suggest new functionalities for fully depleted silicon-on-insulator, and shed light on the debate over the PZR of carrier-depleted nanosilicon.

DOI: 10.1103/PhysRevApplied.11.044010

I. INTRODUCTION

Mechanical stress modifies the electronic structure of solids and gives rise to a change in electrical resistivity, $\Delta\rho$, known as the "piezoresistance" (PZR) [1]. The PZR, which in crystalline solids may be a tensor quantity, is characterized by the coefficient π:

$$\pi = \frac{1}{X}\frac{\Delta\rho}{\rho_0}, \tag{1}$$

where X is the applied stress and ρ_0 is the zero-stress resistivity. In solids whose electronic structure is well described by a simple, spherical band model, the PZR is due mainly to stress-induced changes in the atomic density, and hence to the equilibrium density of free charge carriers [2,3]. However, if the electronic structure consists of multiple degenerate bands at a single point in the Brillouin zone, or multiple valleys, then the stress-induced density changes are typically negligible compared with changes in the density-of-states-weighted effective masses. The PZR is then principally determined by stress-induced changes in the charge-carrier mobility. This is the case for silicon, where stress-induced intervalley charge transfer results in large PZR for n-type material [1,4], and interchange of heavy and light holes yields similarly large PZR in p-type material [1,5]. The latter case is widely exploited in strained-silicon fin FETs [6] to symmetrize the transconductance gain of the n-channel and p-channel transistors in CMOS circuitry [7]. One technologically important case of relevance here is that of p-type silicon in which both current and stress are parallel to the ⟨110⟩ crystal direction, in which case $\pi_{bulk} \approx 70 \times 10^{-11}$ Pa^{-1}.

Unlike bulk crystals, silicon nano-objects such as nanowires [8] can be strongly depleted of free charge carriers by reduction of the doping level to a point where the surface-depletion-layer width, W, is larger than a characteristic dimension of the object, b. In this space-charge-limited-current (SCLC) regime, unusual and varied PZR has been reported, including giant effects up to $\pi \approx 3500 \times 10^{-11}$ Pa^{-1} in nanowires [9,10] and nanomembranes [11,12], and anomalous (i.e., negative) effects comparable in magnitude to π_{bulk} in nanowires [13,14] and nanomembranes [15]. Many other studies, however, report PZR similar in both sign and magnitude to π_{bulk} [16–25], even when $W \gg b$. While some studies are

*alistair.rowe@polytechnique.edu

performed at high stresses, where nonlinearities may be important [13,14,23], most are performed with $X < 100$ MPa, so it is unclear why such a variety of different behaviors have been observed in nominally-very-similar nano-objects [3]. Aside from scientific curiosity, the question is an important one in the context of applications ranging from motion detection in nanoelectromechanical systems [20,26,27] to strained nanosilicon devices [28–30].

Importantly, all prior experiments [1,2,9–25] used dc methods to measure the PZR. In this approach, a dc voltage, V_{ds}, is applied between the source and drain contacts of a device, and its resistance is estimated by measuring the resulting current, I_0. The stress-induced change in the current, ΔI, for a fixed applied voltage can then be used to estimate the π coefficient in Eq. (1) according to $\pi \approx -1/X \times \Delta I/I_0$. While this approach has the advantage of simplicity, it misses important physical effects, as is shown here. In this work a different approach, based on impedance spectroscopy, is used.

Impedance spectroscopy—the study of electrical impedance as a function of frequency, ω, is widely used in solids, liquids, or at interfaces where a space charge is present because it reveals details of charge-relaxation dynamics and transport kinetics [31]. It is particularly well established in electrochemistry [32], but has also found use in organic semiconductors, where the SCLC regime is often encountered [33], and to characterize the SCLC in photoexcited p-n junctions fabricated from both traditional inorganic semiconductors [34,35] and more-novel materials [36].

The principal strength of impedance spectroscopy compared with the dc method for estimating PZR is that it allows measurement of the π coefficient under both *steady-state* and *non-steady-state* conditions, whereas the dc approach reveals only the steady-state PZR. Here it is shown that the steady-state PZR of simple, resistorlike SCLC devices fabricated from fully depleted silicon-on-insulator (FD SOI) is comparable in sign and magnitude to the usual bulk effect [1], in agreement with Refs. [16–25], while giant, anomalous PZR is observed only under non-steady-state conditions. Analysis of the impedance as a function of ω reveals that the crossover between steady-state and non-steady-state conditions is determined by the capture and emission rates of fast electronic traps associated with crystal defects. The giant, anomalous PZR is therefore ascribed to stress-induced changes in these capture and emission rates, which give rise to stress-induced changes in the *nonequilibrium* hole densities. Moreover, the stress-dependent density of trapped charge gives rise to a giant piezocapacitance (PZC), another phenomenon that is inaccessible with dc methods, and is revealed only through impedance spectroscopy.

II. SAMPLE AND MEASUREMENT DETAILS

Standard photolithographic processing methods are used to produce samples from the $b = 2$ μm thick device layer of a 3-in., (001)-oriented FD-SOI wafer (buried-oxide thickness 2 μm, and a handle thickness of 400 μm). The device layer and handle are nonintentionally doped with boron, $p < 1.4 \times 10^{13}$ cm^{-3}. After processing, the wafer is cut to form macroscopically large chips whose long axis is parallel to the ⟨110⟩ crystal direction as shown in Fig. 1(a). As indicated in Fig. 1(b), each chip contains four FD devices whose active area is 50 μm wide and 30 μm long [see Fig. 1(d)], and that have Ohmic contacts and lines that run to large-area pads [2×2 mm^2, visible in Fig. 1(a)] used for external contacting. In addition to the FD devices, each chip contains a silicon strain gauge, shown in Fig. 1(c), and a resistance ladder, shown in the inset in Fig. 1(b).

The resistance ladders are used to measure the specific contact resistivity, ρ_s, of the Ohmic contacts made to the gauges and FD devices by boron implantation ($p = 10^{20}$ cm^{-3}) followed by metallization and postannealing at 450 °C. This yields contacts with $\rho_s = 1.6 \times 10^{-6}$ Ω cm^2, sufficiently low that they do not contribute to the two-terminal resistances of either the strain gauges or the FD devices, so the contact-to-active area-to-contact of the SCLC devices is described by a p++ - p - p++ structure. As indicated in Fig. 1(c), the gauges are formed by uniform implantation of the active arms (vertical in the image) with a boron density of 2×10^{18} cm^{-3}, and by fabrication of a metallic short perpendicular to the active arms, yielding a fully Ohmic device whose PZR is given by π_{bulk}. The gauges can then be used to estimate *in situ* the ⟨110⟩-oriented uniaxial applied stress near the center of the chip.

The FD devices themselves [shown in Fig. 1(d)] are fabricated without modification of the background boron doping density of the FD-SOI device layer, and are the same type of device in which bulk, steady-state PZR was previously found by dc methods [19]. The low doping density of the device layer yields $W \gg b$, so the Ohmic, bulk channel that exists in the gauges (in gray in Fig. 2) is pinched off, and the device layer is fully depleted (see the graphical argument in Fig. 2). An alternative, but equivalent way of viewing this is to note that the relative number of interface defects is greater than the number of free holes. In a native oxide, the surface density of interface defects is typically 10^{12} cm^{-2} [38], yielding a total interface defect count on the active surface areas of 3×10^7. This contrasts with the total number of equilibrium free holes in the active device volume, 8.4×10^4. The two-terminal resistance is then dominated by the 30×50 μm^2 active area and, as for the strain gauges, current flows parallel to the ⟨110⟩ crystal direction. The steady-state current-voltage characteristics are nonlinear despite the Ohmic contacts (see the inset in Fig. 3), a strong indication of the relative absence

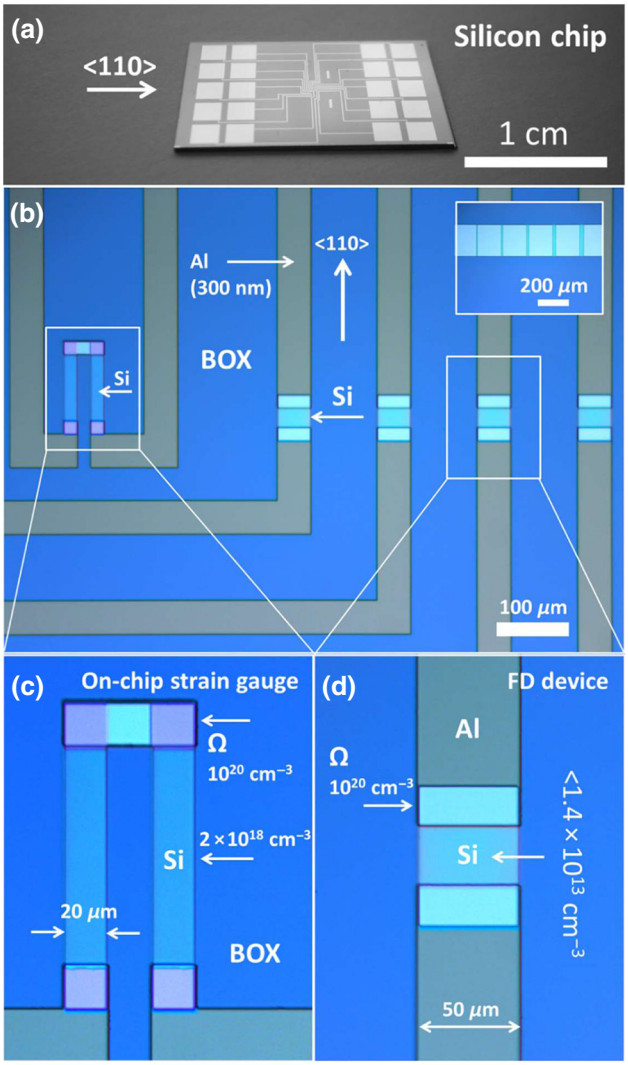

FIG. 1. (a) Photograph of an example silicon chip fabricated for the study. The large contact pads (2×2 mm^2) are visible on the chip, which measures 1.3×2 cm^2. (b) An enlarged microscope image taken at the center of the chip shows the U-shaped strain gauge and four FD devices. The inset shows a resistance ladder used for the measurement of the specific contact resistivity. (c) The on-chip strain gauges. (d) The fully depleted silicon devices. Current flows in the devices and in the on-chip strain gauges parallel to the ⟨110⟩ direction. This is also the direction along which uniaxial stress is applied. BOX, buried oxide. In (c) and (d) the symbol Ω indicates the Ohmic contacts to each of the devices.

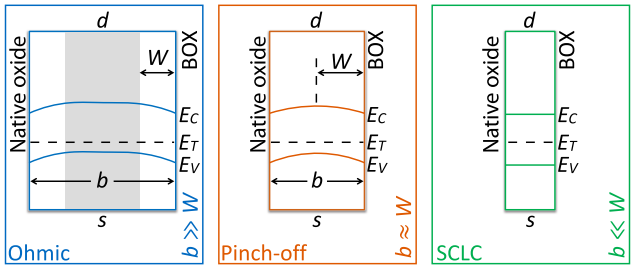

FIG. 2. Side view of the device active area demonstrating the concept of full surface depletion [37]. The active arms of the strain gauges are sufficiently doped so that $W \ll b$ and conduction between the drain (d) and the source (s) is Ohmic (blue box). In the FD devices $W \gg b$, so band bending is absent, and the Fermi level throughout the device is determine by surface pinning at an energy E_T determined by the interface traps. In this limit a SCLC is expected (green box). BOX, buried oxide.

of free holes in equilibrium. Charge transport then occurs in the SCLC regime due to injection of nonequilibrium holes from the anode [39].

Mechanical stress is applied by clamping the left and right ends of the chip in Fig. 1(a) and then pushing along the centerline of the chip (i.e., using a three-point bending method). This method can be used to obtain both uniaxial tensile and compressive stresses on the order of several tens of megapascals, whose magnitude is measured *in situ* with the silicon strain gauge as discussed above. In this way the piezoresponse of the FD devices can be directly compared with that of the strain gauges. It is also noted that the magnitude of the applied stress is modulated between zero and the desired, nonzero value at a frequency on the order of 0.2 Hz so as to avoid any measurement-drift issues [19].

In terms of the electrical measurement, in addition to the advantages presented in Sec. I, impedance spectroscopy is also a natural choice for the estimation of the coefficient π if the device characteristic is nonlinear. This is because a V_{ds}-dependent resistance requires a measurement of the differential conductance. In the following, the in-phase and out-of-phase components of the current resulting from a total applied bias, $V(t) = V_{ds} + V_{\rm ac} \exp i\omega t$, are assimilated with a conductance, G, and a capacitance, C, respectively. Here V_{ds} is the dc component of the applied voltage and $V_{\rm ac}$ is the amplitude of the ac component at frequency ω. In all experiments reported here, $V_{\rm ac} = 1$ V. Both G and C may change with applied stress, V_{ds} and ω, so it is possible to define π coefficients of two types, one for the PZR,

$$\pi_R\,(\omega, V_{ds}) \approx -\frac{1}{X}\frac{\Delta G}{G_0}, \tag{2}$$

where ΔG is the stress-induced change in G and G_0 is the zero-stress conductance, and one for the PZC,

$$\pi_C\,(\omega, V_{ds}) \approx -\frac{1}{X}\frac{\Delta C}{C_0}, \tag{3}$$

where ΔC is the stress-induced change in C and C_0 is the zero-stress capacitance. These equations are valid for small relative changes in G and C, and when stress-induced geometry changes are negligible. The overall

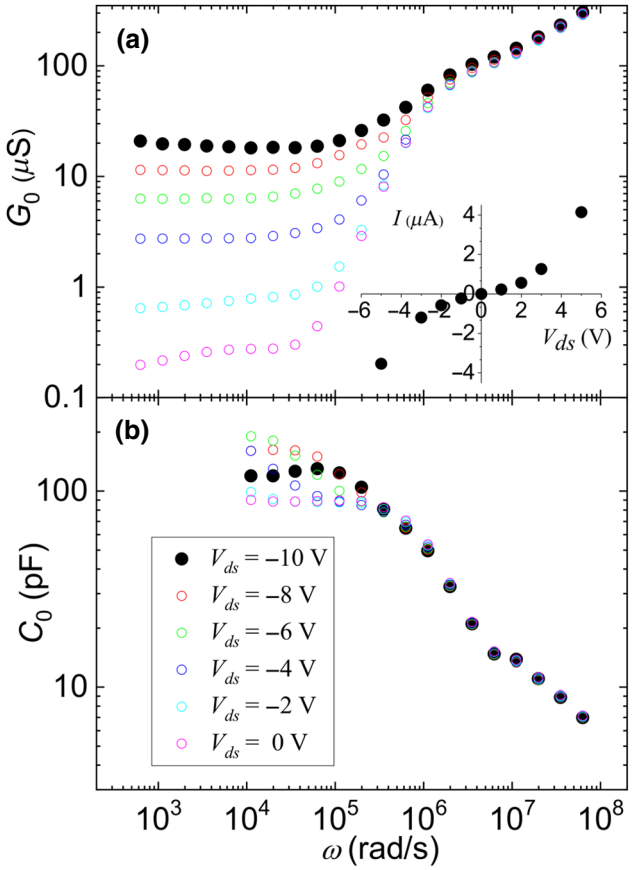

FIG. 3. Zero-stress measurements of G_0 (a) and C_0 (b) as a function of ω and V_{ds}. The inset in (a) shows the steady-state current-voltage characteristic, whose nonlinearity is the first evidence of a SCLC. The frequency variation of G_0 and C_0 is consistent with a SCLC in the presence of fast traps [40]. At low frequencies, capacitance measurements are difficult and the data are not shown.

piezoimpedance coefficient is then

$$\pi_Z(\omega, V_{ds}) = \pi_R \frac{G_0^2}{G_0^2 + \omega^2 C_0^2} + \pi_C \frac{\omega^2 C_0^2}{G_0^2 + \omega^2 C_0^2} + i(\pi_C - \pi_R) \frac{\omega G_0 C_0}{G_0^2 + \omega^2 C_0^2}. \quad (4)$$

The ω-dependent measurements of G and C are made with a commercial impedance analyzer (Hewlett-Packard 4192A LF) with the four-probe (16048A test leads) attachment. Conversion from the four-probe to the two-probe geometry is made approximately 10 cm from the sample holder according to rules outlined in the impedance analyzer user manual (see also the discussion in Appendix A). This conversion is designed to minimize parasitic capacitances in the two-terminal part of the circuit. Importantly, the impedance analyzer's zero correction function is used to account for the conductance and capacitance of the external measurement circuit, thereby ensuring that the measured admittance is that of the device under test only. This is particularly important at frequencies in the 1–10-MHz range, where parasitic resonances can occur. Failure to perform these corrections can result in spurious estimates of the high-frequency PZR and PZC.

III. ZERO-STRESS FD-DEVICE PROPERTIES

Figure 3 shows typical results for the ω and V_{ds} dependence of G_0 and C_0. The increase in G_0 (decrease in C_0) at intermediate frequencies is a signature of small-signal SCLC in the presence of fast electronic traps associated with crystal defects [40]. The values of G_0 and C_0 depend on the device's geometric capacitance (C_g) and conductance (G_g), the source-to-drain transit time (T), and the traps' characteristic capture (ω_c) and emission (ω_e) rates. The strong voltage dependence of G_0 observed at low frequencies is due to the voltage dependence of ω_e, and is discussed further in Sec. V. The frequency dependence of both G_0 and C_0 may be estimated with Kassing's model [40] which provides an approximate analytical solution to a set of coupled differential equations (see Appendix B) that account for a single trap and carrier type. Despite the limitations outlined in Appendix B, the model is nevertheless useful in providing physical insight into the origin of the piezoresponse data presented below. To demonstrate this as simply as possible, Kassing's model is applied to the zero-stress and piezoresponse data obtained for $V_{ds} = 10$ V in the remainder of this work.

Kassing's model yields typical curves given by, for example, the purple lines in Figs. 4(a) and 4(b) for conductance and the capacitance, respectively, at $V_{ds} = 10$ V. The calculated low-frequency-to-high-frequency variation occurring in both quantities around $\omega \approx \omega_c$ is too rapid compared with the data. This is because the FD devices contain a continuous spectrum of traps as indicated by the asymmetric, broad hump centered at about 180 K in the photoinduced-current-transient-spectroscopy (PICTS) signal shown in Fig. 10 in Appendix C. Broad PICTS signals are usually indicative of a continuum of traps whose spectrum is spread by disorder at the silicon/oxide interface [41].

A full description of the trap spectrum is therefore cumbersome, so a compromise solution consisting of the inclusion of a finite number of different trap types is considered. Here six traps represented by the colored curves in Figs. 4(a) and 4(b) are introduced and, as an example of how to apply Kassing's model, the six individual values of G and C for each trap type are calculated for $V_{ds} = 10$ V with use of the trap parameters shown in Table I. A single transit time, $T = 2 \times 10^{-8}$ s, is used for all traps. Similarly, common values of the geometric conductance and capacitance are used for all traps, $G_g = 10^{-4}$ S and $C_g = 6.5 \times 10^{-13}$ F. Six traps was found to be the minimum number necessary to reasonably well match the G_0,

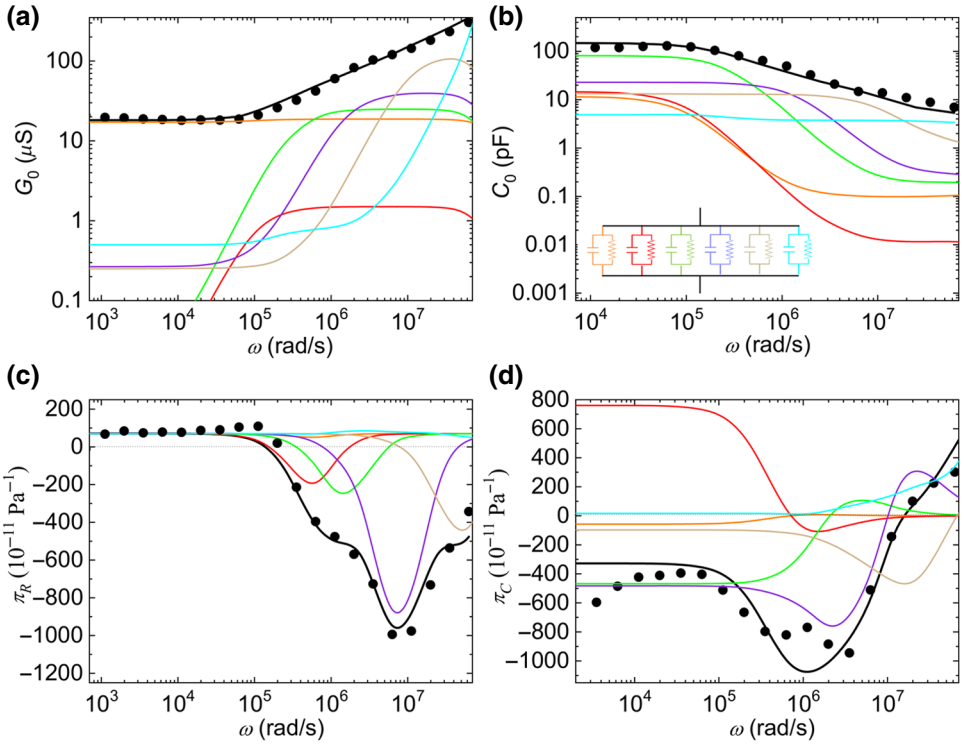

FIG. 4. Simultaneous modeling of zero-stress and piezoresponse data (black circles) obtained as a function of ω for $V_{ds} = 10$ V. (a) The zero-stress conductance, G_0, (b) the zero-stress capacitance, C_0, (c) the PZR π coefficient, π_R, and (d) the PZC π coefficient, π_C. Six individual trap types represented by the colored curves simulate a quasicontinuous trap distribution consistent with the PICTS signal in Appendix C. The individual results are added in parallel [see the inset in (b)] to obtain the overall response (black curves). Fit parameters can be found in Tables I and II.

C_0, π_R, and π_c data *simultaneously* as shown in the following. No claims are made that there are indeed only six trap types in the devices or that the parameter values have a clear physical meaning. The goal is rather to test whether the observed piezoresponse can reasonably be ascribed to the stress dependence of the trapping rates. These points are further discussed in Appendix B. For each trap type, the curve for G and C calculated from Kassing's model is weighted by a prefactor (the *trap weight* in Table I), which represents the relative densities of each of the six traps [see the column with head *relative weight (%)* in Table I]. The overall values of G_0 and C_0 are then found by our adding the individual conductance and capacitance values in parallel as indicated in the inset in Fig. 4(b). It is interesting to note that in all cases except one (trap type 1), the traps are fast ($\omega_e \ll \omega_c$), with the remaining case, depicted in orange in Fig. 4, being slow (i.e., $\omega_c < \omega_e$). As described in Sec. V, this is intimately related to the V_{ds} dependence of the piezoresponse. The choice of parameter values must simultaneously fit both G_0 and C_0 data, so the excellent agreement between the calculated values [black curves in Figs. 4(a) and (b)] and the data [black circles Figs. 4(a) and (b)] is highly satisfactory.

The qualitative picture that emerges is as follows. For $\omega \ll \omega_c$, the applied voltage period is long compared with the lifetime of injected carriers in the band ($2\pi/\omega_c$), so injected, nonequilibrium charge fully relaxes from the band within a voltage cycle (i.e., the free-charge

TABLE I. The fitting parameters used with Kassing's model [40] to calculate G_0 in Fig. 4(a) and C_0 in Fig. 4(b).

Trap number	Line color in Fig. 4	ω_c (rad/s)	ω_e (rad/s)	Trap weight	Relative weight (%)
1	Orange	800	10000	0.19	2.1
2	Red	10^5	100	0.03	0.3
3	Green	3×10^5	100	0.5	5.5
4	Purple	1.5×10^6	5000	0.8	8.9
5	Brown	10^7	10^4	2.5	27.7
6	Cyan	10^8	10^5	5	55.4

population reaches the steady state). Results obtained in this frequency range are therefore directly comparable with those obtained with dc methods. For fast traps it can be shown [40] that the density of the injected charge remaining in the band in the steady state is approximately a factor $\omega_e/\omega_c \ll 1$ smaller than in the trap-free case, and hence G_0 is small and frequency independent,

$$G_0\,(\omega \ll \omega_c) \approx \frac{\omega_e G_g}{\omega_c} \ll G_g, \tag{5}$$

as seen in Fig. 3. Equation (5) is important when we consider the steady-state PZR in Sec. IV. Conversely, a fraction $\omega_c/(\omega_e + \omega_c)$ of the injected charge is trapped during the voltage cycle. It approaches 1 for fast traps and is closer to 0 for slow traps. Any trapped charge increases C_0 relative to C_g, to $C_g/\omega_c T$ [40].

For $\omega \gg \omega_c$, the voltage period is short compared with $2\pi/\omega_c$, so relaxation of injected charge from the band is negligible; in effect, the device behaves as if no traps were present. To within a factor on the order of unity, $G_0 \to G_g$ and $C_0 \to C_g$. The transition between this high-frequency limit and the steady-state limit occurs when $\omega \approx \omega_c$.

IV. PIEZORESPONSE OF THE FD DEVICES

A 25-MPa uniaxial tensile stress is now applied parallel to the ⟨110⟩ crystal direction. Typical results for π_R and π_C are shown in Fig. 5.

To link the impedance-spectroscopy method with the dc techniques used previously, it is useful to begin by comparing the PZR measured in each case on the FD devices studied here. At the lowest frequencies where $\omega \ll \omega_c$ for all trap types shown in Table I, π_R measured by impedance spectroscopy is only weakly dependent on ω, as seen in Fig. 5(a). A weak, quasilinear dependence of π_R on V_{ds} is, however, apparent, and this is seen more clearly in the inset in Fig. 5(a), where the red crosses correspond to the data points obtained at the lowest measurement frequency, $\omega = 1000$ rad/s. These data points are very similar to those obtained with the dc method outlined in Sec. I and shown as black crosses in the inset in Fig. 5(a). The good agreement between the two approaches not only increases confidence in the impedance-spectroscopy piezoresponse measurements but also reinforces the statement in Sec. III that at the lowest measurement frequencies used here, the FD devices are indeed in the steady-state limit.

In the steady state (i.e., $\omega \ll \omega_c$) therefore, π_R is neither giant [9–12] nor anomalous [15]. Aside from an intriguing (but weak) V_{ds} dependence, it is rather similar in sign and magnitude to π_{bulk} [1], consistent with most previous steady-state PZR measurements on silicon nanoobjects made with dc methods [16–25]. In the following we argue [using a combination of Kassing's model and the Shockley-Read-Hall (SRH) model [42]] that if the stress dependence of E_V and E_T shown in Fig. 2 is identical, then

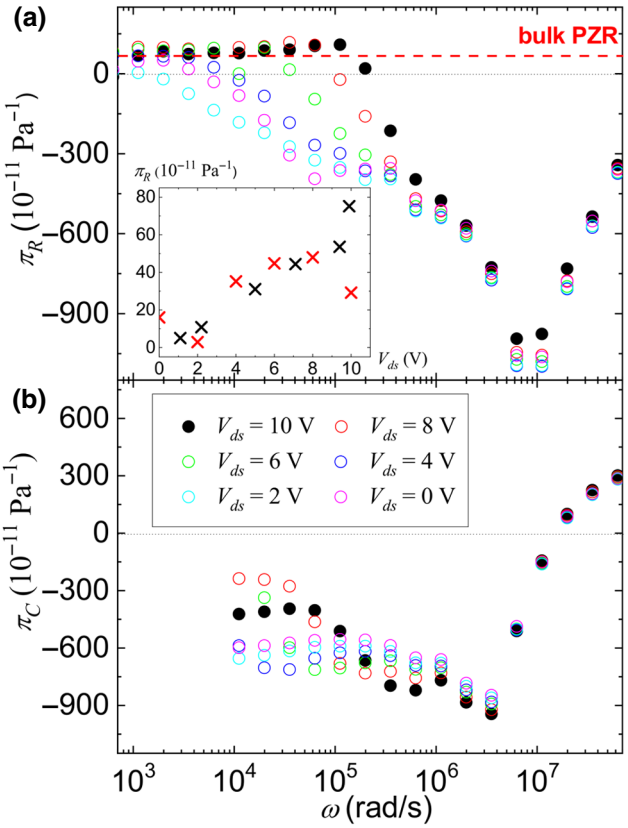

FIG. 5. (a) PZR and (b) PZC as a function of ω for several values of V_{ds} obtained for an applied tensile stress of 25 MPa parallel to the ⟨110⟩ crystal direction. The sign and magnitude of these coefficients are to be compared with those of π_{bulk} [dashed red line in (a)]. The inset in (a) compares the PZR π coefficient measured with dc techniques (black crosses) with that obtained at low frequencies ($\omega < 1000$ rad/s) by impedance spectroscopy (red crosses).

the steady-state PZR should be equal to π_{bulk}, as observed, in the SCLC regime in the presence of fast traps.

The principal effect of mechanical stress in solids is to shift electronic energy levels [43]; the aforementioned stress-induced effective mass change giving rise to bulk PZR of p-type silicon is due, for example, to shifts in the heavy-hole and light-hole valence-band energies [1,5]. Consider for simplicity only the case of hole capture and emission in the SRH model (similar expressions are valid for electrons) [42]. If the equilibrium hole concentration, p_0, is small compared with p_1, the hole concentration obtained when the Fermi level, E_F, is equal to the trap energy, E_T, [42] then in the steady state $\omega_c p \approx \omega_e p_t$ [40,44], where p is the density of holes in the band and p_t is the density of trapped holes. With use of nondegenerate electron statistics, the ratio appearing in Eq. (5) is then

$$\frac{\omega_e}{\omega_c} \propto \exp\left[-\left(E_T - E_V\right)/k_B T\right], \tag{6}$$

were E_V denotes the valence-band-edge energy. Equation (6) shows implicitly how stress-induced changes to ω_c and ω_e result from stress-induced changes to either $E_V - E_F$ or $E_V - E_T$ or both of them. However, according to Eq. (5) for the steady-state conductance, the observation of bulklike steady-state PZR here suggests that while both ω_c and ω_e may change with stress, *their ratio does not*. With the zero-stress values of ω_e and ω_c obtained from measurements of G_0 and C_0 as given in Table I, this imposes constraints on the possible stress dependence of ω_e and ω_c; that is,

$$\frac{1}{\omega_e}\frac{d\omega_e}{dX} = \frac{1}{\omega_c}\frac{d\omega_c}{dX}. \tag{7}$$

Using Eqs. (6) and (7), we can write

$$\frac{dE_V}{dX} = \frac{dE_T}{dX}. \tag{8}$$

This result indicates that if the stress-induced shifts in the valence-band-edge and the trap energies are equal, then the steady-state PZR will not have a component due to stress-induced changes in the trapping and emission rates. Rather it will be given by the usual bulk PZR as observed here.

That said, the PZR does exhibit giant, anomalous behavior, with π_R reaching approximately -1100×10^{-11} Pa^{-1}, but only at intermediate ω corresponding to non-steady-state conditions. The ω dependence of π_R can be understood with use of a stress-dependent version of Kassing's model in which ω_c, ω_e, and T vary with stress. The relative variation of T is assumed to be equal to that of the carrier mobility, yielding $dT/dX = -1.2 \times 10^{-18}$ s/Pa. This change is common to all six trap types. Stress-induced changes to G_g, C_g, and the trap densities (i.e., the relative weights in Table I) are assumed to be negligible. The colored curves in Fig. 4(c) correspond to the calculated PZR of each of the six trap types. The stress dependences of ω_e and ω_c for each trap type are chosen so that ω_e/ω_c is stress independent according to the constraint given by Eq. (7), and they are given in Table II. The overall PZR [black curve in Fig. 4(c)], calculated by our summing the individual contributions, is well matched to data measured at $V_{ds} = 10$ V.

TABLE II. The stress dependence of the fitting parameters used with Kassing's model [40] to calculate the ω dependence of the PZR and the PZC for $V_{ds} = 10$ V in Figs. 4(c) and 4(d), respectively. The values in the last two columns are consistent with the values of ω_e and ω_c given in Table I and the constraint given by Eq. (7).

Trap number	Line color in Fig. 4	$d\omega_c/dX$ (rad/s Pa)	$d\omega_e/dX$ (rad/s Pa)
1	Orange	-1×10^{-5}	-1.25×10^{-4}
2	Red	-7.74×10^{-3}	-7.74×10^{-6}
3	Green	-2.25×10^{-3}	-8.5×10^{-7}
4	Purple	-4.75×10^{-2}	-1.61×10^{-4}
5	Brown	-0.12	-1.2×10^{-4}
6	Cyan	-1	-1×10^{-3}

For G_0, three PZR frequency regimes can be qualitatively described:

(a) The steady-state limit, where results are directly comparable to those obtained using dc methods as discussed above.

(b) The high-frequency limit, $\omega \gg \omega_c$, where injected holes remain in the valence band during the voltage period and the device behaves as if traps were absent. Any stress-induced changes to ω_c and ω_e are therefore irrelevant in this limit, and a relatively small PZR comparable to the bulk p-type value is expected. The measurement apparatus used here is not able to reach this frequency regime, although a significant drop in the PZR is observed at the highest frequencies in Fig. 5.

(c) In the intermediate range, $\omega \approx \omega_c$, only partial relaxation of the nonequilibrium injected charge from the bands to the traps occurs, and any stress-induced change to ω_c and ω_e results in large relative changes to the fraction of this charge that remains in the band during a voltage cycle. Thus the giant, anomalous PZR observed in this frequency regime is due to stress-induced changes to the charge capture dynamics at fast traps. In addition to the stress-induced change to the carrier mobilities, there is then an additional change in the *nonequilibrium* electron and hole densities present in the bands. This is a purely non-steady-state phenomenon and is fundamentally different from stress-induced changes to the *equilibrium* carrier density resulting from the volume density changes discussed in Sec. I.

As shown in Fig. 5(b), the PZC is another phenomenon revealed by impedance spectroscopy that is not accessible with dc methods. Unlike the steady-state PZR, the steady-state PZC is large, with $\pi_C \approx -600 \times 10^{-11}$ Pa^{-1} at $V_{ds} = 0$ V. At higher frequencies it reaches approximately -900×10^{-11} Pa^{-1} before changing sign at the highest frequencies. In Kassing's model there are no longer any free parameters available to determine the PZC; it must be consistent with the parameter values shown in Tables I and II used to model the PZR. Summing of the individual PZC curves shown in Fig. 4(d) for $V_{ds} = 10$ V can, however, be done with an arbitrary sign associated with each curve so as to account for the electronlike or holelike nature of the traps as follows.

The capacitance is given by the ratio $\Delta Q/\Delta V$, where ΔQ is the incremental change in the charge stored in the FD device occurring due to an incremental change in the potential difference from the source to the drain, ΔV. Since the applied stress modifies the density of trapped charge according to the trapping-dynamics arguments

given above, this results in a change in the capacitance. The sign of the trapped charge will therefore determine the sign of the capacitance change with stress. If the trap is an electron trap, a stress-induced reduction in the capture rate (see Table II) will reduce the average density of trapped electrons, resulting in a net positive change in the total trapped charge (and therefore an increase in the capacitance). According to the definition of π_c in Eq. (3), this will yield a negative PZC coefficient. The opposite will be true of hole traps. Thus, the individual PZC curves calculated with the parameters in Tables I and II must be multiplied by a factor of either -1 for hole traps or $+1$ for electron traps. In Fig. 4(d), the red (trap type 2) and cyan (trap type 6) curves have been multiplied by -1 and therefore nominally correspond to hole traps. The other four traps are therefore considered to be electron traps. If the fast traps involved here are the intrinsic Pb_0 interface defects (as the symmetry of the piezoresponse discussed in Sec. VI suggests), this would be consistent with the amphoteric nature of such traps [38,45]. The resulting PZC sum yields an overall calculated π_C at $V_{ds} = 10$ V that is well matched to the experimental curve as shown in Fig. 4(d).

Given the large number of model parameters and the limitations of Kassing's model discussed above, no claims can be made here as to the physical meaning of their values. On the other hand, the ability to simultaneously match all four experimental curves (G_0, C_0, π_R, and π_C) in Fig. 4 with a single set of parameters reinforces the interpretation based on stress-induced changes to the fast trapping dynamics.

With Eq. (4) and the G_0, C_0, π_R, and π_C data, π_Z can be calculated as shown in Fig. 6 for $V_{ds} = 10$ V. At low and high frequency, π_Z is dominated by the PZR. It is imaginary at the highest frequencies, real at the peak piezoresponse, and real at low frequencies (see the gray boxes and labels). This result again emphasizes that in the steady state, the overall piezoresponse is just the bulk PZR. At intermediate frequencies, however, π_Z is dominated by the PZC and switches from an imaginary to a real response with increasing frequency.

The interpretation of the giant, anomalous piezoresponse as being due to stress-induced modifications of the fast trapping dynamics in the SCLC regime is further reinforced by two final observations; the strong, systematic voltage dependence of the PZR below approximately 6×10^5 rad/s shown in Fig. 5(a), and the symmetry of the piezoresponse in stress.

V. VOLTAGE DEPENDENCE OF THE PIEZORESPONSE

It is known that ω_e can be affected by an applied electric field [46], and it is tempting (but difficult) to attribute the V_{ds} dependence of the PICTS signal in Fig. 10 in Appendix C to this. To account for the V_{ds} dependence

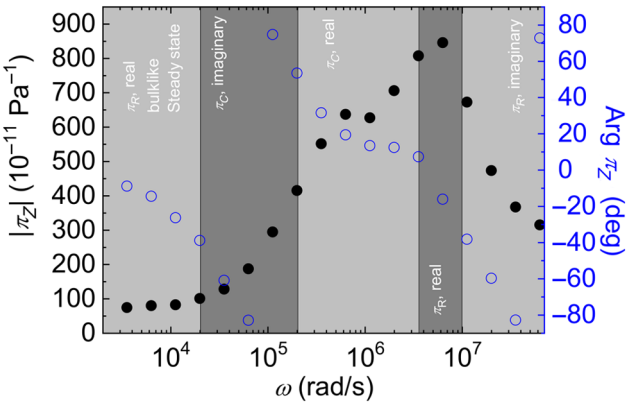

FIG. 6. The amplitude (black circles) and phase (blue circles) of π_Z at $V_{ds} = 10$ V calculated with Eq. 4 from the data presented earlier. π_Z can be real or imaginary, and may be dominated by either the PZR or the PZC depending on ω (see the labels in gray boxes). In the steady state, the overall piezoresponse is close to the usual, bulk PZR given by π_{bulk}.

of the piezoresponse, the emission rates for all six traps used here are allowed to vary with V_{ds} by the same voltage-dependent prefactor, β [46]. Assuming a stress-independent β, then $d\omega_e/dX \rightarrow \beta d\omega_e/dX$. Since the low-frequency conductance is directly proportional to ω_e as in Eq. (5), the voltage dependence of the PZR is the relevant quantity to study. β is chosen for each value of V_{ds} (see Table III) so as to best match the V_{ds} dependence of the lowest-frequency PZR peak (dashed lines for four V_{ds} values in Fig. 7). The resulting overall PZR is shown as solid lines whose color corresponds to that of the data (circles) in Fig. 5. This procedure predicts not only the V_{ds} dependence of the lowest-frequency PZR peak but also the relative insensitivity of the higher-frequency PZR to changes in V_{ds}, although that the emission rates of the higher-capture-rate traps have also been multiplied by β.

As can be seen from the values of ω_c and ω_e in Table I, the relative sensitivity of the low-frequency measurements to V_{ds} arises because the trap with the lowest capture rate (orange lines in Fig. 4) transitions from being a fast trap at $V_{ds} = 0$ V to a slow trap at higher voltages. To make this explicit, consider trap type 1, whose emission rate at $V_{ds} = 0$ V is $87\,750/40 = 2193$ rad/s according to the values of ω_e in Table I and β in Table III. This is less than the capture rate (16 875 rad/s), which is voltage independent, and so a type-1 trap is a fast trap at $V_{ds} = 0$ V. It transitions from being a fast trap to a slow trap for an applied bias

TABLE III. Voltage-dependent prefactors, β, used to account for the increase in all trap emission rates with increasing applied voltage.

V_{ds} (V)	10	8	6	4	2	0
β	40	20	4	2	1.6	1

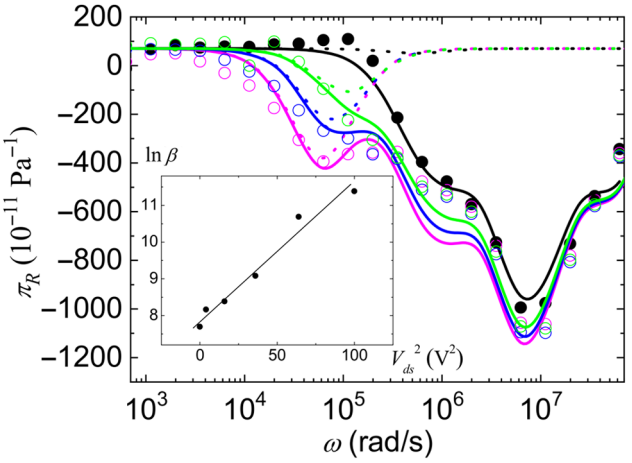

FIG. 7. V_{ds} dependence of the PZR, with the data (circles) shown according to the color scheme of Fig. 5. An applied voltage increases all trap emission rates by a voltage-dependent prefactor β, whose values are chosen so as to best match the low-frequency PZR. The resulting V_{ds}^2 dependence of $\ln\beta$ (see the insert) suggests that the voltage dependence of the PZR results from changes to the trap emission rates arising from phonon-assisted tunneling [46].

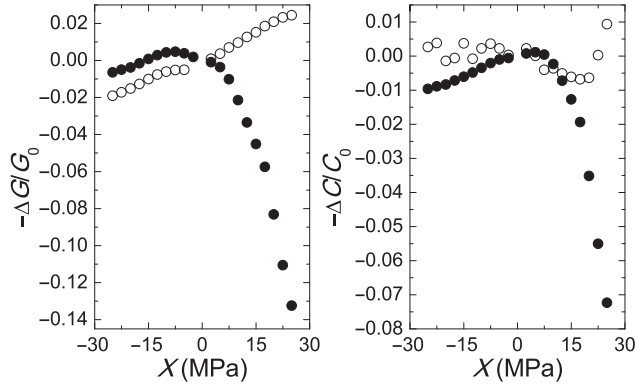

FIG. 8. Stress symmetry of the PZR (left) and the PZC (right) at $\omega = 1.5 \times 10^4$ rad/s (open circles) and at $\omega = 1.5 \times 10^7$ rad/s (filled circles) for $V_{ds} = 10$ V. An odd symmetry is consistent with the usual bulk PZR, while an even symmetry can be attributed to electromechanical activity of intrinsic Pb_0 centers at the silicon/oxide interface.

between 6 and 8 V. Since only fast traps contain nonnegligible charge concentrations and therefore contribute to the anomalous piezoresponse, this provides an explanation for the voltage dependence of the type-1-trap contribution to the PZR. By combining the values from Tables I and III, the reader will see that all the other traps are fast over the experimentally tested range of V_{ds}. This analysis can be pushed further by considering the inset in Fig. 7, in which $\ln\beta$ is plotted against V_{ds}^2. The observed linear variation rules out the Poole-Frenkel effect and favors a phonon-assisted-tunneling emission process [46].

VI. SYMMETRY OF THE PIEZORESPONSE

Figure 8 shows the relative stress-induced changes in G and C at two measurement frequencies, $\omega = 1.5 \times 10^4$ rad/s (open circles) and $\omega = 1.5 \times 10^7$ rad/s (filled circles) for $V_{ds} = 10$ V. Negative values of X correspond to compression. At low frequency, $-\Delta G/G_0$ is approximately linear (i.e., odd) in stress as would be expected for the steady-state, bulk PZR [1]. The stress symmetry of the PZC at low frequency is not clear, partly because capacitance measurements are difficult at such frequencies. Unlike the PZR, however, it is not clearly odd. The high-frequency PZR and PZC are both even (but asymmetric) in stress. This symmetry has been reported elsewhere, including in the gate leakage currents [47] and in flash electrically erasable programable read-only memories [48], and has even been reported in steady-state PZR measurements made with dc techniques on depleted silicon membranes [11,12]. More recently, a theoretical evaluation of the stress dependence of Pb-like trap energies also revealed an even response [49], and spectroscopic studies of the stress dependence of the surface band bending at a silicon/oxide interface was also found to be even in stress [50]. Fig. 8 therefore provides tentative evidence that these defects are the electromechanically active fast traps responsible the non-steady-state piezoresponse. This conclusion is also consistent with the broad PICTS signal shown and discussed in Appendix C (see Fig. 10). Although the literature leaves little doubt about the presence of Pb-like defects at the silicon/oxide interface on a (001) surface, it would be of interest to verify their presence with, for example, electron-spin-resonance techniques [51].

VII. CONCLUSIONS

With use of impedance-spectroscopy techniques the steady-state piezoresponse of the SCLC in natively oxidized nonintentionally-doped, p-type silicon is found to be just the usual bulk PZR. This reinforces most reports of such behavior in depleted, silicon nano-objects [16–25]. Using a combination of the SRH model and Kassing's model for small-signal SCLC, we argue that this is a consequence of similar stress-induced shifts in the valence-band edge, E_V, and the energies of fast traps, E_T, that modify the steady-state conductance. The observations suggest possible explanations for discrepancies in the nanosilicon PZR literature, in particular reports of giant or anomalous effects at small applied stresses in the steady state [9–12,15,52]. One possibility is that in the nano-objects in which giant or anomalous steady-state PZR is reported, E_V and E_T depend differently on applied stress and so Eqs. (6) and (8) are no longer valid. In some of these reports chemical surface treatments were used, which may have significantly modified the surface electronic structure [9,11,12,15] and therefore changed the stress dependence

of E_T. Another possibility is that these measurements were not strictly made in the steady state. If the stress dependence of the I-V characteristic was obtained by rapid sweeping of the applied voltage with a source-measure unit, traps may no longer be able to reach the steady state [53], and the apparent steady-state PZR may in fact be a mixture of the high-frequency PZR and the PZC reported here.

Impedance-spectroscopy methods are, however, shown to give access to the non-steady-state piezoresponse where giant, anomalous PZR is observed. In addition, the quadrature response is found to correspond to a giant PZC. Using a simplified, stress-dependent model of the SCLC in the presence of fast traps, and by observing the voltage dependence of the PZR, we show these phenomena are the result of electromechanically active fast traps whose capture and emission rates are stress dependent. In this case at measurement frequencies $\omega \approx \omega_c$, the PZR consists of not only the stress-induced change in the charge-carrier mobilities [1] (i.e., the bulk effect) but also a significantly larger stress-induced change in the concentration of nonequilibrium holes injected from the Ohmic contacts. The PZC is in some respects complementary to the PZR in that it depends on stress-induced changes to the *trapped*-hole concentrations. The symmetry of the giant, anomalous PZR and the PZC suggest that intrinsic Pb_0 defects at the silicon/oxide interface are the likely candidates for the electromechanically active fast traps.

These observations suggest a number of interesting experiments, including stress-dependent defect spectroscopy to evaluate the stress-induced changes in E_T, studies of the piezoresponse of FD devices into which specific, well-chosen defects have been engineered, studies of the non-steady-state piezoresponse of piezoresistive, nanomechanical oscillators whose resonant frequency is comparable with ω_c [20], and studies of the piezoresponse of transistors in the subthreshold region where SCLCs occur and which are of interest for ultralow-power-consumption applications [52,54]. Moreover, in some proposed quantum devices, fast traps are desirable for device operation [55], while in other cases SCLCs are difficult to avoid (e.g., in organic materials [56–58]). From these examples it is clear that the ability to significantly modify trap-mediated SCLCs with mechanical stress must at the very least be accounted for, and may in fact provide a route to new functionalities.

ACKNOWLEDGMENTS

This work was partially financed by the French Agence Nationale de la Recherche, Contract No. ANR-17-CE24-0005. The authors also thank the CNRS and the University of Melbourne for a travel grant (CNRS PRC "Spectromech").

APPENDIX A: FREQUENCY-DEPENDENT IMPEDANCE MEASUREMENTS

The Hewlett-Packard 4192A impedance analyzer used with a 16048A test lead attachment has a four-terminal configuration as shown in Fig. 9. The attachment consists of four 1-m-long coaxial cables whose line capacitance and resistance are compensated for automatically by the impedance analyzer. In the absence of any other correction, the impedance analyzer reports the impedance of anything attached to these four cables as being due to the device under test.

The SCLC devices measured here are two-terminal devices, so conversion from four to two contacts is necessary, and is done according to Fig. 9. The impedance analyzer then reports a total impedance equal to that of the sample plus excess line impedance combination. To obtain only the sample's impedance, the impedance analyzer has a "ZERO CORRECT" function. Zero correction of the excess line impedance is achieved in two steps. First, the mainly reactive component of the excess line impedance is corrected by removing the sample and using the "ZERO OPEN" function. Second, the mainly resistive component of the excess line impedance is corrected by replacing the sample with a short circuit (in this case a 200-nm-thick gold layer on glass) and using the "ZERO SHORT" function. During this procedure it is important to keep the geometry of the 10-cm coaxial cables as constant as possible, since to do otherwise may change parasitic line impedances. In subsequent measurements with the "ZERO OPEN" and "ZERO SHORT" functions activated, the

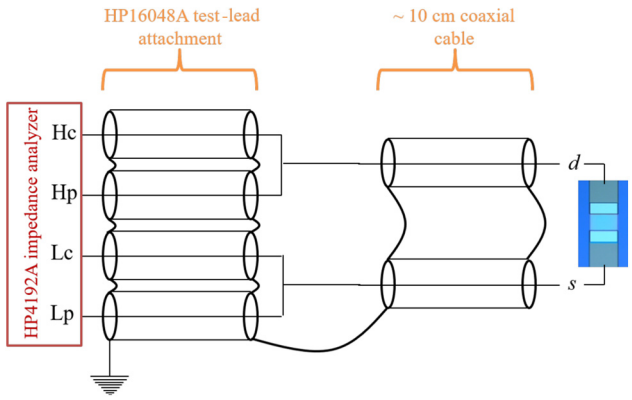

FIG. 9. The four-to-two-terminal-contact conversion used to obtain the impedance of the sample between the source (s) and the drain (d) with an Hewlett-Packard 4192A impedance analyzer with four output terminals, current high (Hc), potential high (Hp), potential low (Lp), and current low (Lc). The impedance of the four 1-m-long coaxial cables making up the HP 16048A test-lead attachment is automatically compensated for, while the correction for the impedance of the added 10-cm coaxial cables is done with the analyzer's "ZERO CORRECT" function.

impedance analyzer reports the impedance of the sample only.

One remaining issue at high frequencies ($\omega > 2\pi \times 1$ MHz) is potential resonances of the combined sample plus excess line impedance load. This can be a difficult issue to solve, and the earth-shield connections shown in Fig. 9 are chosen to try to minimize such effects. Resonances have a typical, strongly peaked frequency dependence accompanied by a rapid change in the phase of the reported impedance. In the measurements reported here, no such behavior is observed, so it is concluded that resonances are not an issue in this case. Observation of any such behavior means that the data cannot be used.

APPENDIX B: LIMITATIONS OF KASSING'S MODEL

As pointed out in Sec. III, Kassing's model [40], which gives a small-signal analysis of a SCLC in the presence of traps, treats a single charge-carrier type (electrons or holes, but not both) and a single trap type. An important simplification in this model is the constant values of ω_c and ω_e given by

$$\omega_c = C_p \frac{N_T - p_{t_0}}{N_T} \tag{B1}$$

and

$$\omega_e = C_p \frac{p_0 + p_1}{N_T}, \tag{B2}$$

where p_{t_0} is the equilibrium trapped-hole density, N_T is the trap density, p_0 is the equilibrium free-hole density, p_1 is the density of holes that would be obtained if the Fermi energy lay at the trap energy ($E_F = E_T$), and C_p is the Shockley-Read capture constant for holes [42]. However, the full equations of motion that describe unipolar SCLC hole transport in the presence of traps are given by the following time-dependent, coupled differential equations in one dimension:

$$E(x,t) = -\frac{\partial V(x,t)}{\partial x}, \tag{B3}$$

$$J(x,t) = p(x,t)\mu_p q E(x,t) + \epsilon_r \epsilon_0 \frac{\partial E(x,t)}{\partial t}, \tag{B4}$$

$$\frac{\partial E(x,t)}{\partial x} = -\frac{q}{\epsilon_r \epsilon_0}\left[p_t(x,t) + p(x,t) - p_{t_0} - p_0\right], \tag{B5}$$

$$\frac{\partial p(x,t)}{\partial t} = -C_p \left\{ p(x,t)\left[\frac{N_t - p_t(x,t)}{N_t}\right] - \frac{p_1}{N_t} p_t(x,t) \right\} + \frac{1}{q}\frac{\partial J(x,t)}{\partial x}, \tag{B6}$$

$$\frac{\partial p_t(x,t)}{\partial t} = C_p \left\{ p(x,t)\left[\frac{N_t - p_t(x,t)}{N_t}\right] - \frac{p_1}{N_t} p_t(x,t) \right\}. \tag{B7}$$

Here the equations are written for holes as applicable to the SCLC devices studied here, but they could equally well be written for electrons. In this set of equations, several terms are recognizable. In Eq. (B4) for the overall current density, $p(x,t)\mu_p q E(x,t)$ is the hole drift-current density, where q is the elemental electronic charge, μ_p is the hole mobility, $p(x,t)$ is the free-electron density, and $E(x,t)$ is the electric field. The second term on the right-hand-side of Eq. (B4) is the displacement current, with $\epsilon_r \epsilon_0$ the permittivity of the medium. In the rate equation for free holes, Eq. (B6), the terms in the curly brackets are the net capture rates of holes as originally defined by Shockley and Read [42], and $p_t(x,t)$ is the trapped-hole density. From study of the Shockley-Read term, a potentially significant simplification (oversimplification?) in Kassing's model is apparent.

The first term in the curly brackets is related to the capture rate. The prefactor multiplying $p(x,t)$ is $C_p[N_T - p_t(x,t)]/N_T$ and can be considered to be a Shockley-Read capture rate $\omega_c^{\mathrm{SRH}}(x,t)$. Unlike Kassing's capture rate given in Eq. (B1), the Shockley-Read capture rate depends on space and time via the spatial and temporal dependence of $p_t(x,t)$. Similarly, the second term in the curly brackets corresponds to a (space- and time-dependent) Shockley-Read emission rate, although a direct comparison with Kassing's (space- and time-independent) expression, Eq. (B2), is less clear. These differences offer a potential explanation for the large number of parameters required to model the experimental data by Kassing's approach.

In this work a minimum of six trap types is required to obtain reasonable agreement between a model based on Kassing's approach and the experimental data. This is necessary to model the relatively slow increase in G_0 with increasing frequency (and similarly for the decrease in C_0) shown in Fig. 3, and suggests (along with the broad, featureless PICTS signal) that the devices contain traps exhibiting a large spectrum of capture and emission rates. To model such a broad spectrum with Kassing's approach, where each trap type has a constant capture and emission rate given by Eqs. (B1) and (B2), respectively, it is evident that multiple trap types must be used. It is known, however, that in the SCLC regime the free-hole concentration, like the trapped-hole concentration, can be an extremely strong function of space and time [59]. Thus, it is possible that a single trap type defined by C_p, N_T, and p_1 might yield a large spectrum of capture and emission rates due to the space and time dependence of the Shockley-Read rates discussed in the previous paragraph.

Evaluation of this possibility requires numerical solution of Eqs. (B3)–(B7) with appropriate boundary conditions in order to calculate the resulting small-signal

impedance as a function of ω. A non-steady-state giant or anomalous piezoresponse would then potentially arise due to a stress dependence of C_p and p_1. Surprisingly, these equations have not been fully treated in the literature, where it is possible to find only unipolar treatments either without traps [40,60–63] or approximate solutions for a single trapping level [40,62,64], including Kassing's work.

APPENDIX C: PHOTOINDUCED-CURRENT-TRANSIENT SPECTROSCOPY

Since the impedance-spectroscopy data suggest that both the zero-stress and the piezoresponse properties of the FD devices are determined by the electromechanical properties of fast electronic traps, initial attempts at defect spectroscopy measurements are made on the FD devices by PICTS. PICTS is a variant of deep-level transient spectroscopy (DLTS) [65], which is used to investigate deep-level traps in high-resistivity materials and devices [41,66,67]. By use of a periodic above-band-gap optical excitation to generate electron-hole pairs, traps are readily filled by photocarriers. Immediately after the end of the optical excitation, a sharp current drop due to recombination is observed, followed by a slower delay due to trapped-charge-carrier emission. By monitoring the detrapping of trapped charge carriers as a function of temperature, one can determine important parameters about the traps present.

Here PICTS signals were obtained with use of a pulsed 940-nm commercial, high-speed light-emitting diode with a rise and fall time of 20 ns. A signal generator (Agilent 33210A) was used to apply a 100-ms pulse to the light-emitting diode at a rate of 1 Hz, which delivered an optical pulse of approximately 55 mW to the sample. In the only PICTS data presented here, V_{ds} is fixed throughout the temperature scan. The resulting photocurrent transient is measured with a custom-built DLTS setup consisting of an Stanford Research Systems SR 570 current amplifier with the temperature ramped from 86 to 300 K in 2-K increments. At each temperature step, 30 transients are averaged to increase the signal-to-noise ratio. The averaged current transients are then processed with a DLTS double-boxcar analysis with times t_1 and t_2 chosen according to $t_2/t_1 = 2$ and $t_1 = 175$ ms to obtain the PICTS signals shown in Fig. 10(a).

Figure 10(a) shows the PICTS signal as a function of V_{ds} displaced vertically with increasing voltage for clarity. For $V_{ds} = 1$ V, a clear peak centered aat 106 K can be seen. The Arrhenius plot in Fig. 10(b) is constructed from a set of PICTS signals obtained with different values of t_1 and t_2, and reveals the trapping level lying approximately 0.182 eV above the valence-band edge. The origin of this discrete trap level is unclear. As V_{ds} is increased, the peak at approximately 106 K disappears. Instead, an asymmetric broad hump centered at 180 K is observed. This continuous nonzero distribution is usually associated with interface states described by a continuum of states within the band gap [41]. It is also noted that increases to V_{ds} significantly shift the broad PICTS signal to lower temperature, and that a change in the shape of the broad distribution is also apparent. It is tempting to ascribe this variation either to the Poole-Frenkel effect or to phonon-assisted tunneling emission from traps [46], but no clear tendency (e.g., in the peak PICTS signal position or in the characteristic PICTS relaxation times) that would permit identification of either phenomenon is evident from the data.

At elevated temperatures, current-transient fluctuations as shown in Fig. 11, likely due to random telegraph noise, start to dominate the current transient. As the

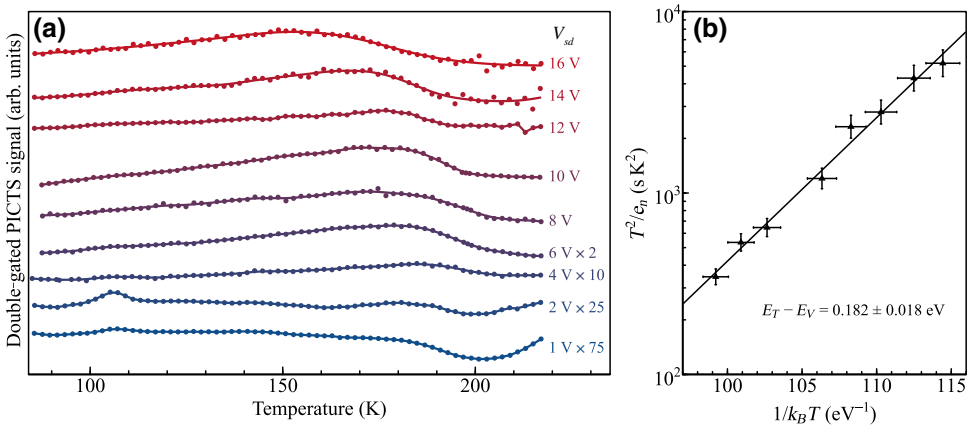

FIG. 10. (a) The PICTS signal obtained as a function of V_{ds} displaced vertically for clarity. A smoothing spline fit is fitted to the raw PICTS data as a guide for the eye. The asymmetric, extended hump visible for $V_{ds} \geq 4$ V is usually associated with a continuous trap distribution that may be associated with silicon/oxide interface states [41]. (b) Arrhenius plot constructed from a set of PICTS signals obtained with different values of t_1 and t_2, revealing that the sharp structure visible at $V_{ds} = 1$ V in (a) corresponds to a trap lying approximately 0.182 eV above the valence-band edge.

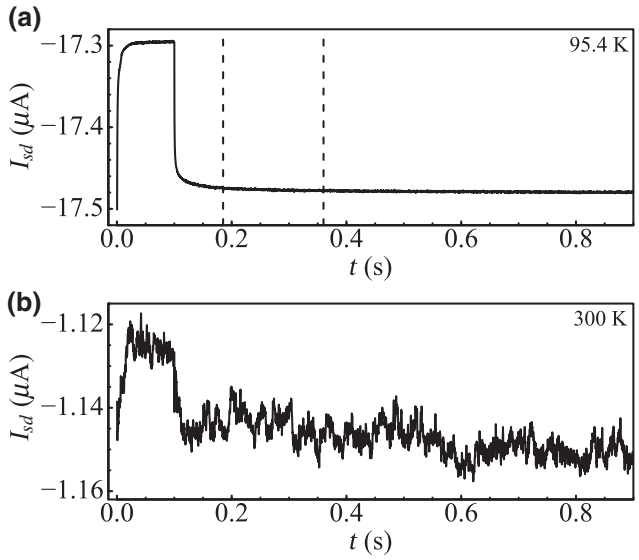

FIG. 11. Raw photoinduced current transients measured at (a) 95.4 K and (b) 300.0 K with $V_{ds} = 6$ V. The clean transient in (a) permits a double-boxcar analysis (dotted lines) that is used to construct the PICTS signal in Fig. 10(a). At elevated temperatures in (b), the amplitude of the random telegraph noise is comparable to that of the photoinduced current transient. Boxcar analysis at high temperatures is therefore avoided.

random-telegraph-noise amplitude is comparable to the current-transient amplitude, double-boxcar analysis used for PICTS is not appropriate. Therefore, useful PICTS signals are restricted to the temperature range from 90 to 220 K, although measurements up to room temperature are performed. Note also that in the room-temperature piezoresponse measurements reported in the main text, the random telegraph noise is averaged out so that only the mean values of the conductance and capacitance are considered.

[1] C. S. Smith, Piezoresistance effect in germanium and silicon, Phys. Rev. **94**, 42 (1954).

[2] A. Sagar, Piezoresistance in *n*-type GaAs, Phys. Rev. **112**, 1533 (1958).

[3] A. C. H. Rowe, Piezoresistance in silicon and its nanostructures, J. Mater. Res. **29**, 731 (2014).

[4] C. Herring and E. Vogt, Transport and deformation-potential theory for many-valley semiconductors with anisotropic scattering, Phys. Rev. **101**, 944 (1956).

[5] J. S. Milne, I. Favorskiy, A. C. H. Rowe, S. Arscott, and Ch. Renner, Piezoresistance in Silicon at Uniaxial Compressive Stresses up to 3 GPa, Phys. Rev. Lett. **108**, 256801 (2012).

[6] J. L. Hoyt, H. M. Nayfeh, S. Eguchi, I. Aberg, G. Xia, T. Drake, E. A. Fitzgerald, and D. A. Antoniadis, in *Electron Devices Meeting, 2002. IEDM'02. International* (IEEE, San Francisco, CA, 2002), p. 23.

[7] J.-J. Lee, S.-T. Hsu, D. J. Tweet, and J.-S. Maa, Strained silicon finFET device, US Patent 7,045,401 (2006).

[8] B. S. Simpkins, M. A. Mastro, C. R. Eddy, Jr., and P. E. Pehrsson, Surface depletion effects in semiconducting nanowires, J. Appl. Phys. **103**, 104313 (2008).

[9] R. He and P. Yang, Giant piezoresistance effect in silicon nanowires, Nat. Nanotechol. **1**, 42 (2006).

[10] P. Neuzil, C. C. Wong, and J. Reboud, Electrically controlled giant piezoresistance in silicon nanowires, Nano Lett. **10**, 1248 (2010).

[11] Y. Yang and X. Li, Giant piezoresistance of *p*-type nanothick silicon induced by interface electron trapping instead of 2D quantum confinement, Nanotechnology **22**, 015501 (2010).

[12] Y. Yang and X. Li, Giant piezoresistance measured in *n*-type nanothick Si layer that has interface with SiO_2, IEEE Electron Device Lett. **32**, 411 (2011).

[13] A. Lugstein, M. Steinmair, A. Steiger, H. Kosina, and E. Bertagnolli, Anomalous piezoresistance effect in ultrastrained silicon nanowires, Nano Lett. **10**, 3204 (2010).

[14] K. Winkler, E. Bertagnolli, and A. Lugstein, Origin of anomalous piezoresistive effects in VLS grown Si nanowires, Nano Lett. **15**, 1780 (2015).

[15] H. Jang, J. Kim, M.-S. Kim, J. H. Cho, H. Choi, and J.-H. Ahn, Observation of the inverse giant piezoresistance effect in silicon nanomembranes probed by ultrafast terahertz spectroscopy, Nano Lett. **14**, 6942 (2014).

[16] T. Toriyama, D. Funai, and S. Sugiyama, Piezoresistance measurement on single crystal silicon nanowires, J. Appl. Phys. **93**, 561 (2003).

[17] K. Reck, J. Richter, O. Hansen, and E. V. Thomsen, in *IEEE 21st International Conference on Micro Electro Mechanical Systems* (IEEE, Tucson, AZ, 2008), p. 717.

[18] T. T. Bui, D. V. Dao, K. Nakamura, T. Toriyama, and S. Sugiyama, in *2009 International Symposium on Micro-Nano Mechatronics and Human Science (MHS 2009)* (IEEE, Nagoya, Japan, 2009), p. 462.

[19] J. S. Milne, A. C. H. Rowe, S. Arscott, and Ch. Renner, Giant Piezoresistance Effects in Silicon Nanowires and Microwires, Phys. Rev. Lett. **105**, 226802 (2010).

[20] E. Mile, G. Jourdan, I. Bargatin, S. Labarthe, C. Marcoux, P. Andreucci, S. Hentz, C. Kharrat, E. Colinet, and L. Duraffourg, In-plane nanoelectromechanical resonators based on silicon nanowire piezoresistive detection, Nanotechnology **21**, 165504 (2010).

[21] T. Barwicz, L. Klein, S. J. Koester, and H. Hamann, Silicon nanowire piezoresistance: Impact of surface crystallographic orientation, Appl. Phys. Lett. **97**, 023110 (2010).

[22] A. Koumela, D. Mercier, C. Dupré, G. Jourdan, C. Marcoux, E. Ollier, S. T. Purcell, and L. Duraffourg, Piezoresistance of top-down suspended Si nanowires, Nanotechnology **22**, 395701 (2011).

[23] U. Kumar Bhaskar, T. Pardoen, V. Passi, and J.-P. Raskin, Piezoresistance of nano-scale silicon up to 2 GPa in tension, Appl. Phys. Lett. **102**, 031911 (2013).

[24] H.-P. Phan, T. Kozeki, T. Dinh, T. Fujii, A. Qamar, Y. Zhu, T. Namazu, N.-T. Nguyen, and D. Viet Dao, Piezoresistive effect of *p*-type silicon nanowires fabricated by a top-down process using FIB implantation and wet etching, RSC Adv. **5**, 82121 (2015).

[25] M. M. McClarty, N. Jegenyes, M. Gaudet, C. Toccafondi, R. Ossikovski, F. Vaurette, S. Arscott, and A. C. H.

Rowe, Geometric and chemical components of the giant piezoresistance in silicon nanowires, Appl. Phys. Lett. **109**, 023102 (2016).
[26] K. L. Ekinci, Electromechanical transducers at the nanoscale: Actuation and sensing of motion in nanoelectromechanical systems (NEMS), Small **1**, 786 (2005).
[27] R. He, X. L. Feng, M. L. Roukes, and P. Yang, Self-transducing silicon nanowire electromechanical systems at room temperature, Nano Lett. **8**, 1756 (2008).
[28] J. W. Ma, W. J. Lee, J. M. Bae, K. S. Jeong, S. H. Oh, J. H. Kim, S. H. Kim, J. H. Seo, J. P. Ahn, H. Kim, and M. H. Cho, Carrier mobility enhancement of tensile strained Si and SiGe nanowires via surface defect engineering, Nano Lett. **15**, 7204 (2015).
[29] I. Olivares, T. Angelova, and P. Sanchis, On the influence of interface charging dynamics and stressing conditions in strained silicon devices, Sci. Rep. **7**, 7241 (2017).
[30] P. Scherpelz and G. Galli, Optimizing surface defects for atomic-scale electronics: Si dangling bonds, Phys. Rev. Mater. **1**, 021602 (2017).
[31] E. Barsoukov and J. R. Macdonald, *Impedance spectroscopy: Theory, experiment, and applications* (John Wiley & Sons, Hoboken, NJ, 2018).
[32] M. E. Orazem and B. Tribollet, *Electrochemical impedance spectroscopy* (John Wiley & Sons, Hoboken, NJ, 2011), Vol. 48.
[33] H. C. F. Martens, H. B. Brom, and P. W. M. Blom, Frequency-dependent electrical response of holes in poly-phenylene vinylene, Phys. Rev. B **60**, R8489 (1999).
[34] V. D. Mihailetchi, J. Wildeman, and P. W. M. Blom, Space-Charge Limited Photocurrent, Phys. Rev. Lett. **94**, 126602 (2005).
[35] I. Mora-Sero, G. Garcia-Belmonte, P. P. Boix, M. A. Vazquez, and J. Bisquert, Impedance spectroscopy characterisation of highly efficient silicon solar cells under different light illumination intensities, Energy Environ. Sci. **2**, 678 (2009).
[36] A. Pockett, G. E. Eperon, T. Peltola, H. J. Snaith, A. Walker, L. M. Peter, and P. J. Cameron, Characterization of planar lead halide perovskite solar cells by impedance spectroscopy, open-circuit photovoltage decay, and intensity-modulated photovoltage/photocurrent spectroscopy, J. Phys. Chem. C **119**, 3456 (2015).
[37] A. C. H. Rowe, Silicon nanowires feel the pinch, Nat. Nanotechol. **3**, 311 (2008).
[38] Y. Nishi, Study of silicon-silicon dioxide structure by electron spin resonance I, Jpn. J. Appl. Phys. **10**, 52 (1971).
[39] M. A. Lampert and A. Rose, Volume-controlled, two-carrier currents in solids: The injected plasma case, Phys. Rev. **121**, 26 (1961).
[40] R. Kassing, Calculation of the frequency dependence of the admittance of SCLC diodes, Phys. Status Solidi (a) **28**, 107 (1975).
[41] G. Papaioannou, V. Ioannou-Sougleridis, S. Cristoloveanu, and C. Jaussaud, Photoinduced current transient spectroscopy in silicon-on-insulator films formed by oxygen implantation, J. Appl. Phys. **65**, 3725 (1989).
[42] W. Shockley and W. T. Read, Jr., Statistics of the recombinations of holes and electrons, Phys. Rev. **87**, 835 (1952).
[43] J. Bardeen and W. Shockley, Deformation potentials and mobilities in non-polar crystals, Phys. Rev. **80**, 72 (1950).
[44] M.-A. Nicolet, H. R. Bilger, and R. J. J. Zijlstra, Noise in single and double injection currents in solids (I), Phys. Status Solidi (b) **70**, 9 (1975).
[45] E. H. Poindexter, G. J. Gerardi, M. E. Rueckel, P. J. Caplan, N. M. Johnson, and D. K. Biegelsen, Electronic traps and p_b centers at the Si/SiO_2 interface: Band-gap energy distribution, J. Appl. Phys. **56**, 2844 (1984).
[46] S. D. Ganichev, E. Ziemann, W. Prettl, I. N. Yassievich, A. A. Istratov, and E. R. Weber, Distinction between the Poole-Frenkel and tunneling models of electric-field-stimulated carrier emission from deep levels in semiconductors, Phys. Rev. B **61**, 10361 (2000).
[47] Y. S. Choi, T. Nishida, and S. E. Thompson, Impact of mechanical stress on direct and trap-assisted gate leakage currents in *p*-type silicon metal-oxide-semiconductor capacitors, Appl. Phys. Lett. **92**, 173507 (2008).
[48] A. Toda, S. Fujieda, K. Kanamori, J. Suzuki, K. Kuroyanagi, N. Kodama, Y. Den, and O. Nishizaka, in *2005 IEEE International Reliability Physics Symposium. Proceedings, 43rd Annual* (IEEE, San Jose, CA, 2005), p. 250.
[49] G. Kovacevic and B. Pivac, Structure,defects, and strain in silicon-silicon oxide interfaces, J. Appl. Phys. **115**, 043531 (2014).
[50] H. Li, L. Martinelli, F. Cadiz, A. Bendounan, S. Arscott, F. Sirotti, and A. C. H. Rowe, Mechanical stress dependence of the Fermi level pinning on an oxidized silicon surface, Appl. Surf. Sci. **478**, 284 (2019).
[51] E. H. Poindexter and P. J. Caplan, Characterization of Si/SiO_2 interface defects by electron spin resonance, Prog. Surf. Sci. **14**, 201 (1983).
[52] T.-K. Kang, Evidence for giant piezoresistance effect in *n*-type silicon nanowire field-effect transistors, Appl. Phys. Lett. **100**, 163501 (2012).
[53] C. Baylis, L. Dunleavy, and W. Clausen, The importance of sweep rate in DC IV measurements, Microw. J. **48**, 130 (2005).
[54] A. Wang, B. H. Calhoun, and A. P. Chandrakasan, *Sub-Threshold Design for Ultra Low-Power Systems* (Springer, Dallas, TX, 2006), Vol. 95.
[55] D. R. McCamey, H. Huebl, M. S. Brandt, W. D. Hutchison, J. C. McCallum, R. G. Clark, and A. R. Hamilton, Electrically detected magnetic resonance inion-implanted Si:P nanostructures, Appl. Phys. Lett. **89**, 182115 (2006).
[56] J. M. Alison and R. M. Hill, A model for bipolar charge transport, trapping and recombination in degassed crosslinked polyethene, J. Phys. D: Appl. Phys. **27**, 1291 (1994).
[57] S. Le Roy, P. Segur, G. Teyssedre, and C. Laurent, Description of bipolar charge transport in polyethylene using a fluid model with a constant mobility: Model prediction, J. Phys. D: Appl. Phys. **37**, 298 (2003).
[58] J. E. Mark, *Polymer Data Handbook* (Oxford University Press, New York, NY, 1999).
[59] N. Mott and R. W. Gurney, *Electronic Processes in Ionic Crystals* (Clarendon Press, New York, NY, 1940).

[60] J. Shao and G. T. Wright, Characteristics of the space-charge-limited dielectric diode at very high frequencies, Solid State Electron. **3**, 291 (1961).

[61] A. Van der Ziel, Low frequency noise suppression in space charge limited solid state diodes, Solid State Electron. **9**, 123 (1966).

[62] D. Dascalu, Small-signal theory of space-charge-limited diodes, Int. J. Electron. **21**, 183 (1966).

[63] G. T. Wright, Transit time effects in the space-charge-limited silicon microwave diode, Solid State Electron. **9**, 1 (1966).

[64] A. Many and G. Rakavy, Theory of transient space-charge-limited currents in solids in the presence of trapping, Phys. Rev. **126**, 1980 (1962).

[65] D. V. Lang, Deep-level transient spectroscopy: A new method to characterize traps in semiconductors, J. Appl. Phys. **45**, 3023 (1974).

[66] J. C. Balland, J. P. Zielinger, C. Noguet, and M. Tapiero, Investigation of deep level sin high-resistivity bulk materials by photo-induced current transient spectroscopy. I. review and analysis of some basic problems, J. Phys. D: Appl. Phys. **19**, 57 (1986).

[67] J. C. Balland, J. P. Zielinger, M. Tapiero, J. G. Gross, and C. Noguet, Investigation of deep levels in high-resistivity bulk materials by photo-induced current transient spectroscopy. II. evaluation of various signal processing methods, J. Phys. D: Appl. Phys. **19**, 71 (1986).